Comp. Meth. Civil Eng., Vol. 2 No. 1 (2011) pp. 21-42

CMCE
Computational Methods in Civil Engineering

Invited Paper

Comparison of two integration schemes for a micropolar plasticity model

M.T. Manzari*, K. Yonten

Department of Civil and Environmental Engineering, The George Washington University, 801 22nd Street NW, Washington, DC 20052, U.S.A.

Received 1 January 2011

Abstract

Micropolar plasticity provides the capability to carry out post-failure simulations of geo-structures due to microstructural considerations and embedded length scale in its formulation. An essential part of the numerical implementation of a micropolar plasticity model is the integration of the rate constitutive equations. Efficiency and robustness of the implementation hinge on the type of integration scheme employed. In this paper, two types of algorithms are developed for a critical-state micropolar plasticity model based on cutting plane and substepping integrations procedures. Performance of the two integration algorithms is first assessed in triaxial and biaxial compression tests at an element level. To evaluate the two integration schemes in a strain localization problem, biaxial compression simulations on a slightly heterogeneous specimen of sand are conducted. In all cases the substepping method performs better than the cutting plane method.

Keywords: Integration schemes; Cutting plane method; Substepping method; Micropolar plasticity model; Granular soil.

1. Introduction

Response of granular soils in the pre-failure regime is successfully captured using realistic constitutive models such as the critical state two-surface plasticity model proposed by Manzari and Dafalias [1,2]. However, beyond the pre-failure regime, during further shearing the heterogenous distributions of void ratio and stresses within the soil mass as well as the boundary conditions may lead to formation of highly localized shear zones. This is commonly known as strain localization phenomenon. The thickness of the localized zone normally depends on the average grain size of the soil. It has been observed that the soil grains may undergo significant rotations within the localized band. The energy dissipation due to grain rotations cannot be accounted for in the constitutive models that are formulated in the framework of classical continuum. Therefore, at the onset of strain localization, numerical simulations using the models that are based on classical continuum framework may face convergence difficulties. A suitable framework for post-failure analyses of granular

* Corresponding author: Fax: (202) 994-0127
E-mail address: manzari@gwu.edu (Majid T. Manzari).

soils is micropolar continuum in which any point of the medium undergoes displacements and rotations. It incorporates the characteristic length that relates the couple-stresses and micro-curvatures in the constitutive model. This approach is used by Manzari and Dafalias [3] to enhance their non-polar version of the model in order to capture the post-failure response of geo-structures.

In order to use the micropolar plasticity model proposed by Manzari and Dafalias [3] in nonlinear finite element analysis for solving boundary value problems the rate constitutive equations must be numerically integrated over a discrete sequence of time steps. The integration schemes and the algorithms used in the simulations control the accuracy, convergence and stability characteristics of the global iterative solution. Therefore, an appropriate integration scheme with its proper implementation is important for the overall efficiency and robustness of the numerical simulation code. Generally, a robust implementation requires implicit integration which for a realistic constitutive model can be fairly lengthy and cumbersome. Therefore, explicit and semi-explicit integration schemes may be attractive alternatives to the implicit schemes.

Implicit integration schemes such as Closest Point Projection Method (CPPM) have become popular because it provides unconditionally stable integration of plasticity models [4]. Implicit integration schemes are successfully used for integration of various constitutive models for soils [5-10]. With implicit integration schemes a quadratic convergence and unconditional stability for Newton-Rhapson iterations can be obtained with the use of consistent (algorithmic) tangent operator. While stability and quadratic convergence are guaranteed for simple classical plasticity models such as J_2-plasticity, this may not be true for more complex models. The second derivatives of the yield and plastic potential function are needed in the algorithm as well as for the formation of the consistent tangent operator. It is often lengthy and cumbersome procedure to obtain the closed-form derivatives for complex models, if they can be derived at all, and their implementation is not always straightforward.

In the explicit integration schemes higher order derivatives of yield and plastic potential functions are not needed and the implementation of the algorithms is generally easy and straightforward. While its simplicity and general applicability seem to be attractive features, a major drawback of explicit integration schemes is that the algorithm is conditionally stable which means that an appropriate step size must be used to retain numerical stability. Due to this limitation, explicit schemes are usually less efficient than implicit schemes.

In recent years a new class of explicit integration schemes has been proposed that includes automatic substepping and error control techniques to alleviate the problem of step size requirement. In this category the one that has been popularly used in the past years is that proposed by Sloan [11], and the enhanced and complete form is presented by Sloan *et al* [12]. Two schemes that are generally applicable to elastoplastic constitutive models are presented by Sloan *et al* [12]. One approach is based on a modified Euler method and the other is based on the high order Runge-Kutta formula. The first scheme is recently used for integration of more complex models and is shown to be accurate and efficient both at the element and structural levels [13-16].

Another type of integration scheme is the semi-explicit methods, such as the cutting plane method proposed by Simo and Ortiz [17]. The simplicity and efficiency of this method are quite attractive. However, its major deficiency lies in the weak enforcement of the consistency condition that often produce drift-off errors.

In this paper two integrations schemes, cutting plane method (CPM) and the substepping method (SSM) based on the second order modified Euler method are considered for the integration of the micropolar plasticity model proposed by Manzari and Dafalias [3]. These two algorithms are implemented in the widely used commercial finite element code, ABAQUS, via the user-defined subroutine, UMAT. The performance of the two integration

schemes is first evaluated in one-element simulations. To evaluate the performance of the two schemes in problems involving strain localization, drained and globally undrained biaxial compression tests on a slightly heterogenous granular soil specimen are considered.

2. Micropolar plasticity model

A brief description of this constitutive model, previously proposed by Manzari and Dafalias [3], are outlined in the following subsections.

2.1. Elastic response

Assuming a small perturbation the additive decomposition of the strain and curvature tensors denoted by $\boldsymbol{\varepsilon}$ and $\boldsymbol{\kappa}$, respectively, are given by $\dot{\boldsymbol{\varepsilon}} = \dot{\boldsymbol{\varepsilon}}^e + \dot{\boldsymbol{\varepsilon}}^p$ and $\dot{\boldsymbol{\kappa}} = \dot{\boldsymbol{\kappa}}^e + \dot{\boldsymbol{\kappa}}^p$ where the subscripts "e" and "p" indicate the elastic and plastic components, respectively.
The general isotropic elastic relationship for a micropolar continuum are given by [18]

$$\dot{\boldsymbol{\sigma}}'_{ij} = \lambda \dot{\boldsymbol{\varepsilon}}^e_{kk}\delta_{ij} + 2G\dot{\boldsymbol{\varepsilon}}^e_{(ij)} + 2G_c\dot{\boldsymbol{\varepsilon}}^e_{\{ij\}}; \quad \dot{\mu}_{ij} = \alpha\dot{\kappa}^e_{kk}\delta_{ij} + 2\beta\dot{\kappa}^e_{(ij)} + 2\gamma\dot{\kappa}^e_{\{ij\}} \tag{1}$$

in which the subscript "(ij)" and "{ij}" of the strain and curvature tensors denote the symmetric and skew symmetric parts, respectively. Four additional elastic constants are introduced in addition to the usual Lame constants. To simplify the elastic stress-strain relations we assume $\alpha = \beta = 0$ and $2\gamma = \left(4GG_c\right)\ell_1^2 / \left(G + G_c\right)$ where ℓ_1 is a characteristic length scale and G_c is a material constant. Thus equations (1) is reduced to

$$\dot{\boldsymbol{\sigma}}'_{ij} = \lambda \dot{\boldsymbol{\varepsilon}}^e_{kk}\delta_{ij} + (G + G_c)\dot{\boldsymbol{\varepsilon}}^e_{ij}; \quad \dot{\mu}_{ij} = 2\gamma\dot{\kappa}^e_{ij} \tag{2}$$

In the non-polar version of Dafalias-Manzari model a hypoelastic relation is adopted for a more realistic behavior of granular soils in which shear modulus G is not only a function of pressure, but also a function of current void ratio e and is given by

$$G = G_0 p_{at} \frac{\left(2.97 - e\right)^2}{1 + e}\left(\frac{p'}{p_{at}}\right)^{1/2} \tag{3}$$

where G_0 is a material constant and p_{at} is the reference pressure for normalization, usually the atmospheric pressure.

2.2. Yield function

The yield function is given by

$$f = \left[\tilde{J}_2\right]^{1/2} - \sqrt{2/3}\,p'm = 0 \tag{4}$$

where m represents the size of the yield surface. Here $\tilde{J}_2$, unlike that in the non-polar version of the model, takes the form

$$\tilde{J}_2 = a_1\tilde{s}_{ij}\tilde{s}_{ij} + a_2\tilde{s}_{ij}\tilde{s}_{ji} + b_1\mu_{ij}\mu_{ij} + b_2\mu_{ij}\mu_{ji} \tag{5}$$

where $\tilde{\mathbf{s}} = \mathbf{s} - p\boldsymbol{\alpha};\ \mathbf{s} = \boldsymbol{\sigma}' - p\mathbf{I}$, and here the back-stress tensor $\boldsymbol{\alpha}$ is unsymmetric. The four parameters a_1, a_2, a_3 and a_4 may be obtained considering the micromechanics of particles displacements and rotation in a granular material [19]. Here assuming $a_1 = 1;\ a_2 = 0;\ b_1 = 1/\ell_2^2;\ b_2 = 0$, $\tilde{J}_2$ is simplified to $\tilde{J}_2 = \tilde{s}_{ij}\tilde{s}_{ij} + \left(\mu_{ij}\mu_{ij}\right)/\ell_2^2$ where ℓ_2 is a second characteristic length corresponding to plastic deformation. Although we can set $\ell_2 = \ell_1$ in the present formulation we keep the option of assigning different values to these length scales. The derivatives of the yield function with respect to force-stress and couple-stress tensors are given as

$$\mathbf{L}^{\sigma} = \frac{\partial f}{\partial \boldsymbol{\sigma}} = \mathbf{n}^{\sigma} - \frac{1}{3}N^{\sigma}\mathbf{I};\quad \mathbf{n}^{\sigma} = \frac{\tilde{\mathbf{s}}}{\left[\tilde{J}_2\right]^{1/2}};\quad N^{\sigma} = \mathbf{n}^{\sigma} : \boldsymbol{\alpha} + \sqrt{\frac{2}{3}}m \tag{6}$$

and

$$\mathbf{L}^{\mu} = \frac{\partial f}{\partial \boldsymbol{\mu}} = \mathbf{n}^{\mu} = \frac{b_1\boldsymbol{\mu}}{\left[\tilde{J}_2\right]^{1/2}} \tag{7}$$

The dilatancy, critical, and bounding surfaces can be written as

$$\boldsymbol{\alpha}_{\theta}^{s} = \sqrt{2/3}\alpha_{\theta}^{s}\mathbf{n}^{\sigma};\ \alpha_{\theta}^{s} = g(\theta,c)M\exp(\mp n^{s}\Psi) - m \tag{8}$$

where $\mathbf{n}^{\sigma} = \tilde{\mathbf{s}}/\left(\tilde{J}_2\right)^{1/2}$, the superscript s = b, c, and d, in which b is for bounding surface, c for critical state surface, and d is for dilatancy surface. $\mp$ corresponds to s = b and d, respectively, and $n^c = 0$. The surfaces are dependent on the Lode angle θ through the relation

$$g(\theta,c) = \frac{2c}{(1+c) - (1-c)\cos(3\theta)} \tag{9}$$

where $c = M_e/M_c$ in which M_e and M_c are the critical shear stress ratios in triaxial extension and compression, respectively. The Lode angle is defined by

$$\cos 3\theta = \sqrt{6}tr\mathbf{n}^3;\ \mathbf{n} = \frac{\mathbf{r} - \boldsymbol{\alpha}}{\left[(\mathbf{r} - \boldsymbol{\alpha}) : (\mathbf{r} - \boldsymbol{\alpha})\right]^{1/2}};\ \mathbf{r} = \frac{\mathbf{s}}{p'} \tag{10}$$

where θ varies from 0 to $\pi/3$ as the loading transitions from triaxial compression to extension, and "**:**" denotes the tensor contraction.

Note that the in the calculation of the θ Lode angle only symmetric part of the deviatoric stress tensor is used, and θ is assumed to be independent of the couple-stress tensor.

A novel feature of the model is the incorporation of critical state behavior through the use of the state parameter $\Psi = e - e_c$ which is a measure of how far the material state, i.e, void ratio, is from the critical state. The critical void ratio is given by

$$e_c = e_0 - \lambda_c\left(\frac{p_c}{p_{at}}\right)^{\xi} \tag{11}$$

where e_0, p_c, p_{at} are initial void ratio, pressure at critical state, and atmospheric pressure for normalization respectively, and finally λ_c and ξ are material constants. The bounding and dilatancy surfaces are function of the state parameter Ψ as shown in equation (8). The latter

feature allows the model to be used with a single set of model parameters for all confining pressures and densities.

2.3. Flow rule

The flow rule is non-associative for the plastic strain, but it is assumed to be associative for the plastic curvature:

$$\begin{aligned} \dot{\boldsymbol{\varepsilon}}^p &= \left\langle \dot{\Lambda} \right\rangle \mathbf{R}^\sigma; \quad \mathbf{R}^\sigma = \mathbf{n}^\sigma + \frac{1}{3}\mathbf{DI} \\ \dot{\boldsymbol{\kappa}}^p &= \left\langle \dot{\Lambda} \right\rangle \mathbf{R}^\mu; \quad \mathbf{R}^\mu = \mathbf{L}^\mu \end{aligned} \tag{12}$$

where $\dot{\Lambda} \geq 0$ is a non-negative plastic multiplier, and $\langle\ \rangle$ is the Macaulay bracket which is defined by $\left\langle \dot{\Lambda} \right\rangle = \dot{\Lambda}$, *if* $\dot{\Lambda} > 0$ and 0 for all other values of $\dot{\Lambda}$. The magnitude of plastic strain and curvature tensor is provided by $\dot{\Lambda}$ while the direction of the plastic flow is given by $\mathbf{R}^\sigma$ and $\mathbf{R}^\mu$. D is the dilatancy which is defined in the following section.

2.4. Hardening laws

The hardening laws are similar to those used in the non-polar version, and they are assumed to be independent of the couple-stress tensor. The force-stress, back-stress, and fabric-dilatancy tensors are asymmetric. The back-stress tensor $\boldsymbol{\alpha}$ evolves as follows

$$\dot{\boldsymbol{\alpha}} = \left\langle \dot{\Lambda} \right\rangle \overline{\boldsymbol{\alpha}} \tag{13}$$

where

$$\overline{\boldsymbol{\alpha}} = \frac{2}{3} h \left(\boldsymbol{\alpha}_\theta^b - \boldsymbol{\alpha} \right); \ h = \frac{b_0}{\left(\boldsymbol{\alpha} - \boldsymbol{\alpha}_{in} \right) : \mathbf{n}^\sigma} \tag{14}$$

in which

$$\boldsymbol{\alpha}_\theta^b = \sqrt{\frac{2}{3}} \left[g(\theta, c) M_c \exp(-n^b \Psi) - m \right] \mathbf{n}^\sigma; \ b_0 = G_0 h_0 \left(1 - c_h e \right) \left(\frac{p'}{p_{at}} \right)^{-1/2} \tag{15}$$

and $\boldsymbol{\alpha}_{in}$ is the initial value of $\boldsymbol{\alpha}$ at initiation of a new loading process and is updated when the denominator in the definition of h (equation 14) becomes negative. h_0, c_h, n^b are model parameters.
The evolution of the fabric-dilatancy tensor is given as [3]:

$$\dot{\mathbf{z}} = -c_z \left\langle -\dot{\varepsilon}_v^p \right\rangle \left(z_{\max} \mathbf{n}^\sigma + \mathbf{z} \right) \tag{16}$$

Substituting $\dot{\varepsilon}_v^p = \left\langle \dot{\Lambda} \right\rangle D$ in equation (16) we have the familiar form

$$\dot{\mathbf{z}} = \left\langle \dot{\Lambda} \right\rangle \overline{\mathbf{z}}; \qquad \overline{\mathbf{z}} = -c_z \left\langle -D \right\rangle \left(z_{\max} \mathbf{n}^\sigma + \mathbf{z} \right) \tag{17}$$

in which c_z and z_{max} are model parameters. The former controls the pace of evolution of z in equation (16) while the latter represents the maximum value z can attain. D is also a function of the fabric tensor and is defined by

$$D = A_d \left(\boldsymbol{\alpha}_\theta^d - \boldsymbol{\alpha} \right) : \mathbf{n}^\sigma \tag{18}$$

where

$$\boldsymbol{\alpha}_\theta^d = \sqrt{\frac{2}{3}} \left[g(\theta, c) M_c \exp(n^d \Psi) - m \right] \mathbf{n}^\sigma; \quad A_d = A_0 \left(1 + \left\langle \mathbf{z} : \mathbf{n}^\sigma \right\rangle \right) \tag{19}$$

3. Incremental stress-strain relations

A general form of the elastoplastic constitutive equations in rate form can be obtained in the standard procedure utilizing the essential components of the model discussed in previous sections. The equations are derived as:

$$\begin{bmatrix} \dot{\sigma}'_{ij} \\ \dot{\mu}_{ij} \end{bmatrix} = D^{ep}_{ijkl} \begin{bmatrix} \dot{\varepsilon}_{kl} \\ \dot{\kappa}_{ij} \end{bmatrix}; \quad \begin{bmatrix} \dot{\boldsymbol{\sigma}}' \\ \dot{\boldsymbol{\mu}} \end{bmatrix} = \mathbf{D}^{ep} \begin{bmatrix} \dot{\boldsymbol{\varepsilon}} \\ \dot{\boldsymbol{\kappa}} \end{bmatrix} \tag{20}$$

where

$$D^{ep}_{ijkl} = \begin{bmatrix} \mathcal{D}^{ep}_{ijkl} & \mathcal{L}^{ep}_{ijkl} \\ \mathcal{E}^{ep}_{ijkl} & \mathcal{M}^{ep}_{ijkl} \end{bmatrix}; \quad \mathbf{D}^{ep} = \begin{bmatrix} \boldsymbol{\mathcal{D}}^{ep} & \boldsymbol{\mathcal{L}}^{ep} \\ \boldsymbol{\mathcal{E}}^{ep} & \boldsymbol{\mathcal{M}}^{ep} \end{bmatrix} \tag{21}$$

The four components of $\mathbf{D}^{ep}$ is given as follows

$$\boldsymbol{\mathcal{D}}^{ep} = \mathbf{D}^e_\varepsilon - \frac{\left(\mathbf{D}^e_\sigma : \mathbf{R}^\sigma \right) \otimes \left(\mathbf{L}^\sigma : \mathbf{D}^e_\sigma \right)}{K_p + \mathbf{L}^\sigma : \mathbf{D}^e_\sigma : \mathbf{R}^\sigma + \mathbf{L}^\mu : \mathbf{D}^e_\mu : \mathbf{R}^\mu} \tag{22}$$

$$\boldsymbol{\mathcal{L}}^{ep} = -\frac{\left(\mathbf{D}^e_\sigma : \mathbf{R}^\sigma \right) \otimes \left(\mathbf{L}^\mu : \mathbf{D}^e_\mu \right)}{K_p + \mathbf{L}^\sigma : \mathbf{D}^e_\sigma : \mathbf{R}^\sigma + \mathbf{L}^\mu : \mathbf{D}^e_\mu : \mathbf{R}^\mu} \tag{23}$$

$$\boldsymbol{\mathcal{E}}^{ep} = -\frac{\left(\mathbf{D}^e_\mu : \mathbf{R}^\mu \right) \otimes \left(\mathbf{L}^\sigma : \mathbf{D}^e_\sigma \right)}{K_p + \mathbf{L}^\sigma : \mathbf{D}^e_\sigma : \mathbf{R}^\sigma + \mathbf{L}^\mu : \mathbf{D}^e_\mu : \mathbf{R}^\mu} \tag{24}$$

$$\boldsymbol{\mathcal{M}}^{ep} = \mathbf{D}^e_\mu - \frac{\left(\mathbf{D}^e_\mu : \mathbf{R}^\mu \right) \otimes \left(\mathbf{L}^\mu : \mathbf{D}^e_\mu \right)}{K_p + \mathbf{L}^\sigma : \mathbf{D}^e_\sigma : \mathbf{R}^\sigma + \mathbf{L}^\mu : \mathbf{D}^e_\mu : \mathbf{R}^\mu} \tag{25}$$

where the superscript "ep" refer to "elastoplastic," and "$\otimes$"denotes the tensor product. The second terms in equations (22) and (25) and those in equations (23) and (24) are the terms that appear during plastic yielding in which $\mathbf{L}$ and $\mathbf{R}$ are respectively the derivatives of the yield function and plastic potential function with respect to $\boldsymbol{\sigma}'$ or $\boldsymbol{\mu}$ indicated by the corresponding superscript used. K_p is the plastic modulus. $\mathbf{D}^e_\sigma$ and $\mathbf{D}^e_\mu$ are tensors of elastic constants for elastic relationship where "e" denotes "elastic" and the subscripts denotes the relation corresponding to force-stress or couple-stress. They are given as

$$\mathbf{D}^e_\sigma = \lambda \mathbf{I}_2 \otimes \mathbf{I}_2 + 2G\mathbf{I}^{sym}_4 + 2G_c \mathbf{I}^{skw}_4 \tag{26}$$

$$\mathbf{D}^e_\mu = 2\gamma \mathbf{I}_2 \otimes \mathbf{I}_2 \tag{27}$$

where the $\mathbf{I}_4^{sym} = \left(\delta_{ik}\delta_{jl} + \delta_{il}\delta_{jk}\right)/2$, and $\mathbf{I}_4^{skw} = \left(\delta_{ik}\delta_{jl} - \delta_{il}\delta_{jk}\right)/2$ are the symmetric and skew symmetric fourth rank identity tensor, respectively, and $\mathbf{I}_2 = \delta_{ij}$ is the second rank identity tensor. The plastic modulus is given by $K_p = -\left(\partial f / \partial \boldsymbol{\alpha}\right) \cdot \bar{\boldsymbol{\alpha}}$.

4. Integration schemes

The constitutive model is integrated using the cutting-plane and sub-stepping algorithms. It is convenient to combine together the components of strain and curvature tensors, and the components of force-stress and couple-stress tensors into a single vector in the vector-matrix representation (for implementation purpose) of the second and fourth order tensors, respectively. The following notations are used to indicate the combined variables: $\hat{\boldsymbol{\varepsilon}} = \left\langle \boldsymbol{\varepsilon} \;\; \boldsymbol{\kappa} \right\rangle^T$, $\hat{\boldsymbol{\sigma}} = \left\langle \boldsymbol{\sigma}' \;\; \boldsymbol{\mu} \right\rangle^T$, $\mathbf{L} = \left\langle \mathbf{L}^{\sigma} \;\; \mathbf{L}^{\mu} \right\rangle^T$, $\mathbf{R} = \left\langle \mathbf{R}^{\sigma} \;\; \mathbf{R}^{\mu} \right\rangle^T$. $\hat{\mathbf{D}}^e$ also combines the respective elastic constants which is given in the Appendix. Thus in this section "stress" includes both force-stress and couple-stress, and "strain" includes curvature as well. The two algorithms are described in the next subsections.

4.1. Cutting-plane method

A schematic illustration of cutting plane method is shown in Figure 1. In the cutting-plane method the first step involves an elastic predictor in which a trial stress is calculated by assuming an elastic response. This state of stress may fall inside the yield surface in which case the response is elastic. However, if the predicted stress state lies outside the yield surface in order to satisfy the consistency condition the stress state must be corrected and brought on the yield surface. To state it mathematically

$$\dot{f} = 0 \Rightarrow \mathbf{L} : \dot{\hat{\boldsymbol{\sigma}}} + \frac{\partial f}{\partial \boldsymbol{\alpha}} \dot{\boldsymbol{\alpha}} = 0 \tag{28}$$

Substituting the hardening law $\dot{\boldsymbol{\alpha}} = \dot{\Lambda} \bar{\boldsymbol{\alpha}}$, plastic modulus, and $K_p = -\left(\partial f / \partial \boldsymbol{\alpha}\right) \bar{\boldsymbol{\alpha}}$ in equation (28), we can express it compactly as

$$\dot{f} = \mathbf{L} : \dot{\hat{\boldsymbol{\sigma}}} + \dot{\Lambda} K_p = 0 \tag{29}$$

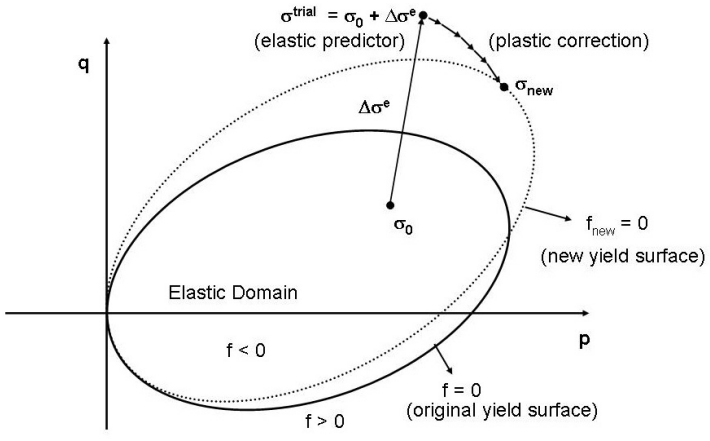

Figure 1. Schematic illustration of Cutting Plane Method.

Now using a Taylor series expansion the first order approximation of the yield function may be written as

$$\delta f = f_0 + \mathbf{L} : \delta\hat{\boldsymbol{\sigma}} + \delta\Lambda K_p = 0 \tag{30}$$

where f_0 is the value of yield function obtained at the current stress state. Assuming no change in the total strain increment during plastic corrector step we substitute the relationship between stress and plastic strain, i.e. $\delta\hat{\boldsymbol{\sigma}} = -\hat{\mathbf{D}}^e : \delta\Lambda\left(\mathbf{R}\right)$, in equation (30) and derive the plastic multiplier as

$$\delta\Lambda = \frac{f_0}{K_p + \mathbf{L} : \hat{\mathbf{D}}^e : \mathbf{R}} \tag{31}$$

The stress state and internal variables are then brought onto the yield surface by generation of plastic strain and internal variables whose magnitudes and direction are given by $\delta\Lambda$ and the tensors $\mathbf{R}$, $\boldsymbol{\alpha}$ and $\mathbf{z}$. However, because of the linearization of the Taylor series expansion of the consistency condition the stress state may not always lie on the yield surface so an iterative procedure has to be used.

The main steps of the algorithm at t_{n+1} time increment and iteration, k, are as follows:

1. Initialize:

   $$k = 0;\ \Delta\hat{\boldsymbol{\varepsilon}}_{n+1}^{p(0)} = 0;\ \boldsymbol{\alpha}_{n+1}^{(0)} = \boldsymbol{\alpha}_n;\ \ \mathbf{z}_{n+1}^{(0)} = \mathbf{z}_n;\ \Lambda_{n+1}^{(0)} = 0$$

2. Calculate trial stresses:

   $$\hat{\boldsymbol{\sigma}}_{n+1}^{(k)} = \hat{\boldsymbol{\sigma}}_n + \Delta\hat{\boldsymbol{\sigma}}^e = \hat{\boldsymbol{\sigma}}_n + \left(\hat{\mathbf{D}}^e\right)_{n+1}^{(k)} : \left(\Delta\hat{\boldsymbol{\varepsilon}}_{n+1} - \Delta\hat{\boldsymbol{\varepsilon}}_{n+1}^{p(k)}\right) = \hat{\boldsymbol{\sigma}}_{n+1}^{trial} - \left(\hat{\mathbf{D}}^e\right)_{n+1}^{(k)} : \Delta\hat{\boldsymbol{\varepsilon}}_{n+1}^{p(k)}$$

   where

   $$\hat{\boldsymbol{\sigma}}_{n+1}^{trial} = \hat{\boldsymbol{\sigma}}_n + \left(\hat{\mathbf{D}}^e\right)_{n+1}^{(k)} : \Delta\hat{\boldsymbol{\varepsilon}}_{n+1}$$

3. Calculate and check if yield condition is satisfied:

   $$f_{n+1}^{(k)} = \left[\left(\tilde{J}_2\right)_{n+1}^{(k)}\right]^{1/2} - \sqrt{\frac{2}{3}}\left(p_{n+1}^{(k)}\right)m$$

   IF $f_{n+1}^{(k)} \le fTol$ then EXIT

   ELSE

4. Compute plastic multiplier:

   $$\Delta\Lambda_{n+1}^{(k)} = \frac{f_{n+1}^{(k)}}{\left(K_p\right)_{n+1}^{(k)} + \mathbf{L}_{n+1}^{(k)} : \left(\hat{\mathbf{D}}^e\right)_{n+1}^{(k)} : \mathbf{R}_{n+1}^{(k)}}$$

   $$\left(K_p\right)_{n+1}^{(k)} = -\left(\frac{\partial f}{\partial \boldsymbol{\alpha}}\right)_{n+1}^{(k)} : \bar{\boldsymbol{\alpha}}_{n+1}^{(k)}$$

5. Update plastic strain and internal variables:

   $$\Delta\hat{\boldsymbol{\varepsilon}}_{n+1}^{p(k+1)} = \Delta\hat{\boldsymbol{\varepsilon}}_{n+1}^{p(k)} + \Delta\Lambda_{n+1}^{(k)}\mathbf{R}_{n+1}^{(k)}$$

   $$\boldsymbol{\alpha}_{n+1}^{(k)} = \boldsymbol{\alpha}_{n+1}^{(k)} + \Delta\Lambda_{n+1}^{(k)}\bar{\boldsymbol{\alpha}}_{n+1}^{(k)}$$

   $$\mathbf{z}_{n+1}^{(k)} = \mathbf{z}_{n+1}^{(k)} + \Delta\Lambda_{n+1}^{(k)}\bar{\mathbf{z}}_{n+1}^{(k)}$$

   $$\Lambda_{n+1}^{(k+1)} = \Lambda_{n+1}^{(k)} + \Delta\Lambda_{n+1}^{(k)}$$

   Set $k \to k+1$ and GOTO Step 2.

4.2. Substepping method

A schematic illustration of the substepping method is shown in Figure 2. The automatic substepping method proposed by Sloan *et al* [12] can be summarized in four key steps. In the first step the trial stress state is calculated by assuming it to be elastic. If the trial stress state is on or inside the yield surface the stress state is updated with the trial stress state.

However, if the trial stress state is outside the yield surface plastic yielding has occurred and thus the yield surface intersection with the stress path must be determined which is the second step. This is done by finding a scalar parameter indicating the proportion of the total strain increment that produces plastic yielding. To satisfy the yield function the current stress state that lies outside the yield surface is scaled by a factor whose value is obtained by either solving the single non-linear equation of the yield function in a closed-form or numerically using methods such as bisection, regula-falsi, secant, Pegasus, etc. The scalar parameter takes the inclusive value between 0 and 1, where the two extreme values represent pure plastic or elastic deformation, respectively.

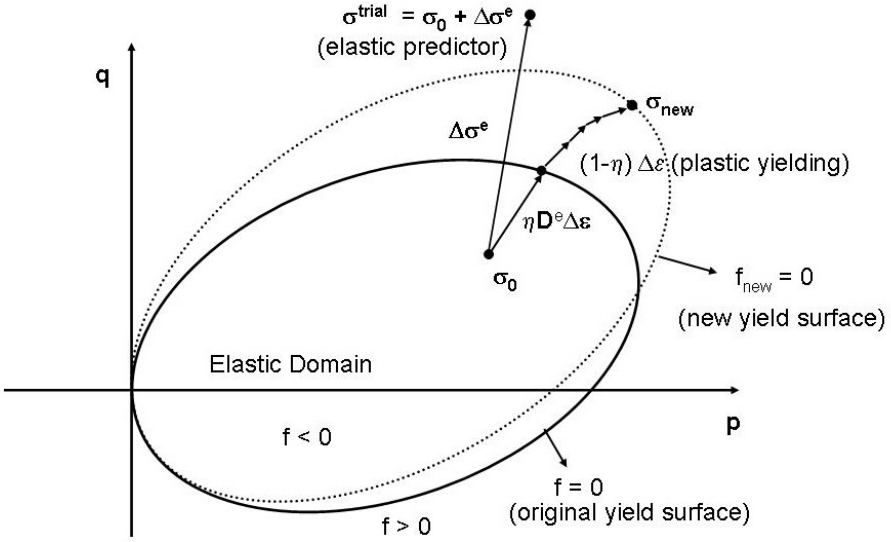

Figure 2. Schematic illustration of the Substepping Method.

The actual stress integration is then carried out in the third step. In this step automatic substepping and an error control algorithm are used. A local error measure that represents errors in the stresses and internal variables due to the approximate integration is computed at each subincrement by taking the difference between the second order accurate modified Euler solution and the first order accurate Euler solution. Based on the dominant error term the next step size is determined thus allowing variable step size throughout the integration process.

Depending on the constitutive model and the nature of the problem being solved the final stress state may lie outside the updated yield surface. This yield surface drift must be corrected by projecting the stress back onto the yield surface to avoid inaccuracy and numerical difficulties that may arise at the global level.

The substepping algorithm is given in the following steps at t_{n+1} time increment and iteration k:

1. Initialize:

$$k = 0;\ T^{(0)} = 0;\ \Delta T^{(0)} = 1;\ \boldsymbol{\alpha}_{n+1}^{(0)} = \boldsymbol{\alpha}_n;\ \mathbf{z}_{n+1}^{(0)} = \mathbf{z}_n$$

2. Calculate trial stresses:

$$\hat{\boldsymbol{\sigma}}_{n+1}^{(k)} = \hat{\boldsymbol{\sigma}}_{n+1}^{trial} = \hat{\boldsymbol{\sigma}}_n + \Delta\hat{\boldsymbol{\sigma}}^e = \hat{\boldsymbol{\sigma}}_n + \left(\hat{\mathbf{D}}^e\right)_{n+1}^{(k)} : \Delta\hat{\boldsymbol{\varepsilon}}_{n+1}$$

where $\left(\hat{\mathbf{D}}^e\right)_{n+1}^{(k)}$ is the secant elastic modulus tensor.

3. Evaluate the yield function and see if it is satisfied:
   IF $f_{n+1}^{(k)}\left(\hat{\boldsymbol{\sigma}}_{n+1}^{trial}, \boldsymbol{\alpha}_{n+1}^{(k)}\right) \le fTol$ EXIT
   ELSE
4. IF $f_{n+1}^{(k)}\left(\hat{\boldsymbol{\sigma}}_n, \boldsymbol{\alpha}_n\right) < -fTol$ and $f_{n+1}^{(k)}\left(\hat{\boldsymbol{\sigma}}_{n+1}^{trial}, \boldsymbol{\alpha}_{n+1}^{(k)}\right) > fTol$ (Elastic-to-plastic transition):
   Calculate the intersection parameter η by solving the equations

$$f_{n+1}^{(k)}\left(\hat{\boldsymbol{\sigma}}_n + \hat{\mathbf{D}}^e\left(\hat{\boldsymbol{\sigma}}_n, \eta\left(\Delta\boldsymbol{\varepsilon}_v\right)_n\right) : \left(\eta\Delta\hat{\boldsymbol{\varepsilon}}_{n+1}\right), \boldsymbol{\alpha}_{n+1}^{(k)}\right) = 0$$

   ELSEIF $\left|f_{n+1}^{(k)}\left(\hat{\boldsymbol{\sigma}}_n, \boldsymbol{\alpha}_n\right)\right| \le fTol$ *and* $f_{n+1}^{(k)}\left(\hat{\boldsymbol{\sigma}}_{n+1}^{trial}, \boldsymbol{\alpha}_{n+1}^{(k)}\right) > fTol$ (purely plastic)
   Set $\eta = 0$
   Update stress and the total strain increment portion that causes plastic yielding

$$\hat{\boldsymbol{\sigma}}_{n+1}^{(k)} = \hat{\boldsymbol{\sigma}}_n + \hat{\mathbf{D}}^e\left(\hat{\boldsymbol{\sigma}}_n, \eta\left(\Delta\boldsymbol{\varepsilon}_v\right)_n\right) : \left(\eta\Delta\hat{\boldsymbol{\varepsilon}}_{n+1}\right)$$

$$\Delta\hat{\boldsymbol{\varepsilon}}_{n+1} = \left(1-\eta\right)\Delta\hat{\boldsymbol{\varepsilon}}_{n+1}$$

5. WHILE T < 1 Repeat (6-13):
6. Calculate the first and second order estimates of the increments of stresses and internal variables as follows:
   Using $\left(\hat{\boldsymbol{\sigma}}_1\right)_{n+1}^{(k)} = \hat{\boldsymbol{\sigma}}_{n+1}^{(k)}$, $\left(\boldsymbol{\alpha}_1\right)_{n+1}^{(k)} = \boldsymbol{\alpha}_{n+1}^{(k)}$ and $\left(\mathbf{z}_1\right)_{n+1}^{(k)} = \mathbf{z}_{n+1}^{(k)}$ calculate the first order increment of stresses and internal variables

$$\left(\Delta\hat{\boldsymbol{\sigma}}_1\right)_{n+1}^{(k)} = \left(\hat{\mathbf{D}}_1^{ep}\right)_{n+1}^{(k)} : \Delta\hat{\boldsymbol{\varepsilon}}_{n+1}^{(k)}$$

   where $\left(\hat{\mathbf{D}}^{ep}\right)_{n+1}^{(k)}$ is the continuum tangent modulus defined in the next section.

$$\left(\Delta\boldsymbol{\alpha}_1\right)_{n+1}^{(k)} = \left(\Delta\Lambda_1\right)_{n+1}^{(k)}\left(\overline{\boldsymbol{\alpha}}_1\right)_{n+1}^{(k)}$$

$$\left(\Delta\mathbf{z}_1\right)_{n+1}^{(k)} = \left(\Delta\Lambda_1\right)_{n+1}^{(k)}\left(\overline{\mathbf{z}}_1\right)_{n+1}^{(k)}$$

$$\Delta\hat{\boldsymbol{\varepsilon}}_{n+1}^{(k)} = \Delta T^{(k)}\Delta\hat{\boldsymbol{\varepsilon}}_{n+1}$$

   in which:

$$\left(\Delta\Lambda_1\right)_{n+1}^{(k)} = \frac{\left(\mathbf{L}_1\right)_{n+1}^{(k)} : \left(\hat{\mathbf{D}}_1^e\right)_{n+1}^{(k)} : \Delta\boldsymbol{\varepsilon}_{n+1}^{(k)}}{\left(K_{p1}\right)_{n+1}^{(k)} + \left(\mathbf{L}_1\right)_{n+1}^{(k)} : \left(\hat{\mathbf{D}}_1^e\right)_{n+1}^{(k)} : \left(\mathbf{R}_1\right)_{n+1}^{(k)}}$$

$$\left(K_{p1}\right)_{n+1}^{(k)} = -\left(\frac{\partial f}{\partial\boldsymbol{\alpha}_1}\right)_{n+1}^{(k)} \cdot \overline{\boldsymbol{\alpha}}_{n+1}^{(k)}$$

   Update the stresses and state variables:

$$\left(\hat{\boldsymbol{\sigma}}_2\right)_{n+1}^{(k)} = \hat{\boldsymbol{\sigma}}_{n+1}^{(k)} + \left(\Delta\hat{\boldsymbol{\sigma}}_1\right)_{n+1}^{(k)}$$

$$\left(\boldsymbol{\alpha}_2\right)_{n+1}^{(k)} = \boldsymbol{\alpha}_{n+1}^{(k)} + \left(\Delta\boldsymbol{\alpha}_1\right)_{n+1}^{(k)}$$

$$\left(\mathbf{z}_2\right)_{n+1}^{(k)} = \mathbf{z}_{n+1}^{(k)} + \left(\Delta\mathbf{z}_1\right)_{n+1}^{(k)}$$

   Using the updated stresses and internal variables calculate the second order increment of stresses and internal variables repeating the same steps used for the calculation of the first order increments.

7. Calculate new stresses and internal variables and temporarily store them:

$$\tilde{\boldsymbol{\sigma}}_{n+1}^{(k)} = \hat{\boldsymbol{\sigma}}_{n+1}^{(k)} + \frac{1}{2}\left(\left(\Delta\hat{\boldsymbol{\sigma}}_1\right)_{n+1}^{(k)} + \left(\Delta\hat{\boldsymbol{\sigma}}_2\right)_{n+1}^{(k)}\right)$$

$$\tilde{\boldsymbol{\alpha}}_{n+1}^{(k)} = \boldsymbol{\alpha}_{n+1}^{(k)} + \frac{1}{2}\left(\left(\Delta\boldsymbol{\alpha}_1\right)_{n+1}^{(k)} + \left(\Delta\boldsymbol{\alpha}_2\right)_{n+1}^{(k)}\right)$$

$$\tilde{\mathbf{z}}_{n+1}^{(k)} = \mathbf{z}_{n+1}^{(k)} + \frac{1}{2}\left(\left(\Delta\mathbf{z}_1\right)_{n+1}^{(k)} + \left(\Delta\mathbf{z}_2\right)_{n+1}^{(k)}\right)$$

8. Calculate relative error, $R_{n+1}^{(k)}$:

$$R_{n+1}^{(k)} = \frac{1}{2}\max\left\{\frac{\left\|\Delta\hat{\boldsymbol{\sigma}}_2 - \Delta\hat{\boldsymbol{\sigma}}_1\right\|}{\left\|\tilde{\boldsymbol{\sigma}}\right\|}, \frac{\left\|\Delta\boldsymbol{\alpha}_2 - \Delta\boldsymbol{\alpha}_1\right\|}{\left\|\tilde{\boldsymbol{\alpha}}\right\|}, \frac{\left\|\Delta\mathbf{z}_2 - \Delta\mathbf{z}_1\right\|}{\left\|\tilde{\mathbf{z}}\right\|}, EPS\right\}\Bigg|_{n+1}^{(k)}$$

where EPS is a machine constant indicating the smallest relative error.

IF $R_{n+1}^{(k)} > STOL$, then the substep has failed and a smaller pseudo-time step needs to be computed by means of an extrapolation. STOL is a user-specified tolerance with a value normally in the range 10^{-3}-10^{-5}. First compute

$$q = \max\left\{0.9\sqrt{STOL / R_{n+1}^{(k)}}, 0.1\right\}$$

and then set

$\Delta T \leftarrow \max\left\{q\Delta T, \Delta T_{\min}\right\}$ GOTO Step 5

ELSE

9. Update stresses and internal variables:

$$\hat{\boldsymbol{\sigma}}_{n+1}^{(k)} = \tilde{\boldsymbol{\sigma}}_{n+1}^{(k)};\ \ \boldsymbol{\alpha}_{n+1}^{(k)} = \tilde{\boldsymbol{\alpha}}_{n+1}^{(k)};\ \ \mathbf{z}_{n+1}^{(k)} = \tilde{\mathbf{z}}_{n+1}^{(k)}$$

10. Use drift correction if $\left|f_{n+1}^{(k)}\left(\hat{\boldsymbol{\sigma}}_{n+1}^{(k)}, \boldsymbol{\alpha}_{n+1}^{(k)}\right)\right| > fTol$

11. Extrapolate the size of the next substep:

$$q = \min\left\{0.9\sqrt{STOL / R_{n+1}^{(k)}}, 1.1\right\}$$

If the previous step failed, limit the step size growth further by enforcing

$$q = \min\left\{q, 1\right\}$$

Update pseudo-time and compute new step size:

$$\Delta T^{(k+1)} = q\Delta T^{(k)};\ T^{(k+1)} = T^{(k)} + \Delta T^{(k)}$$

12. Minimize step size:

$$\Delta T^{(k+1)} = \max\left\{\Delta T^{(k+1)}, \Delta T_{\min}\right\}$$

$$\Delta T^{(k+1)} = \min\left\{\Delta T^{(k+1)}, 1 - \Delta T^{(k+1)}\right\}$$

where $\Delta T_{\min} \le \Delta T^{(k+1)} \le 1$ must hold true.

Set $k \to k+1$ GOTO Step 4

13. At T=1 exit with updated stresses and internal variables.

4.3. Continuum Jacobian

The continuum Jacobian is derived following the same procedure as in the classical continuum utilizing the consistency condition, flow rule, hardening laws, and stress-strain relationship. It is computed after the integration step is successfully completed with the updated stresses and internal variables passed to the global finite element routine to update

the global stiffness matrix and residual force vector. The continuum Jacobian for the micropolar constitutive model takes the form presented in equation (21).

5. Performance of the integration schemes

5.1. One element simulations

To evaluate the performance of the two implemented integration schemes, triaxial compression tests are simulated using a single axisymmetric element. Although the micro-rotations at the bottom nodes may be fixed for bottom nodes in a finite element mesh with more elements, in a single element case fixing the micro-rotations leads to over-constrained system. After the isotropic consolidation of the specimen vertical displacement is applied to the top nodes of the element to shear the specimen. The vertical displacement is applied in several numbers of steps, i.e., varying the increment of strain. The finite element formulation used in these simulations is fully coupled and utilizes mixed elements that couple displacements, micro-rotation, and pore water pressure (u-p-ϕ elements). Both drained and globally undrained simulations are conducted. In the globally undrained simulations, the water flux is prevented from all sides of the specimen.

The force-displacement plots for the two integration schemes in drained and undrained conditions are shown in Figures 3 and 4, respectively. In the drained case up to 50 steps can be used for the substepping method and the results are almost identical to those obtained with 2000 steps. There is a slight difference in results at the peak of the curve because more data points are needed to capture the peak. However, the solution does not converge for the cutting plane method, if the number of steps is not larger than 300. For the undrained case about 100 steps could give as accurate results as larger steps for the substepping method while for the cutting-plane there is a significant difference in the solution between 150 steps and 500 steps. These simulations clearly demonstrate that the substepping method is more robust and efficient than the cutting-plane method.

For both the drained triaxial and biaxial compression simulations iso-error maps are constructed to compare the errors in estimated stress states using the substepping and cutting-plane methods. In both the triaxial and biaxial simulations first the specimen is isotropically consolidated by applying a confining pressure of 100 kPa. Then in the second step the specimen is sheared to bring it to plastic stage. The strain probes of different sizes were imposed by simultaneously applying displacements in horizontal and vertical directions. For each strain probe the exact solution is obtained by dividing the desired displacement increment into 1000 steps. The error, δ, is calculated by using:

$$\delta = \frac{\sqrt{\left(\boldsymbol{\sigma}-\boldsymbol{\sigma}^{*}\right):\left(\boldsymbol{\sigma}-\boldsymbol{\sigma}^{*}\right)}}{\left(\boldsymbol{\sigma}^{*}:\boldsymbol{\sigma}^{*}\right)} \tag{32}$$

where $\boldsymbol{\sigma}^{*}$ is the exact solution and $\boldsymbol{\sigma}$ is the calculated stress tensor for the strain probe. Figures 5 and 6 show the iso-error maps for the two integration schemes, respectively. The computed iso-error maps show same order of magnitude for the biaxial simulations conducted by using the two integration schemes, but the error of substepping method is much smaller than that of the cutting-plane method. For both methods the largest error occurs in tension when the horizontal and vertical strain increments are greater than 65 times the vertical yield strains. Vertical yield strain is used for normalization because it has much larger value than that of the horizontal component. The largest value of the error for substepping method is about 0.25% while for the cutting plane method it is about 0.4 %. Note that the patterns of the iso-error maps are different for the two methods.

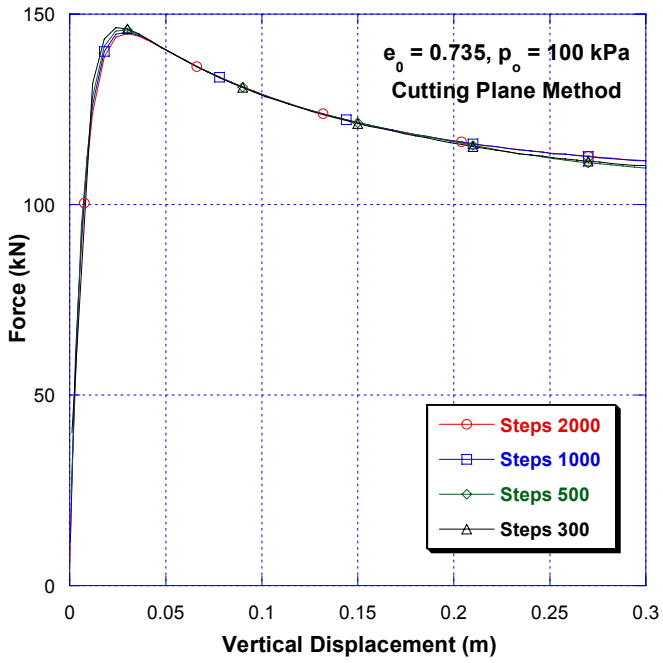

(a)

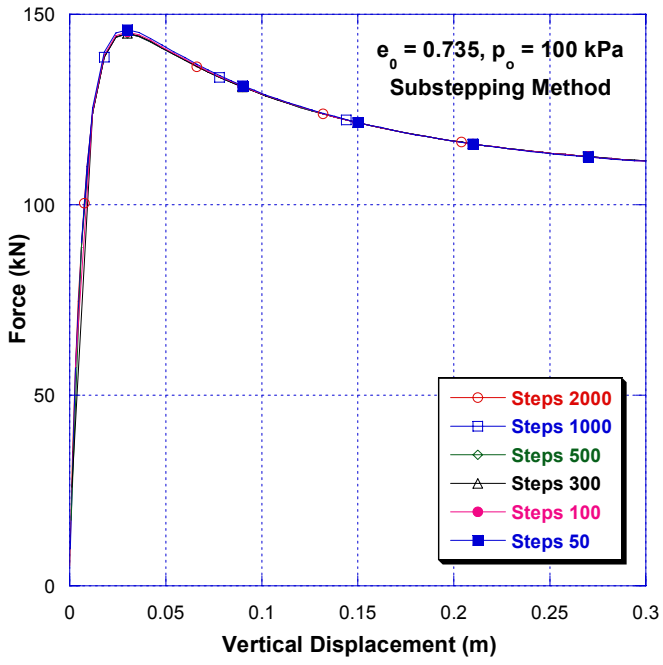

(b)

Figure 3. Force-displacement plots for drained triaxial compression simulations using a micropolar model: (a) Cutting-Plane Method, (b) Substepping Method.

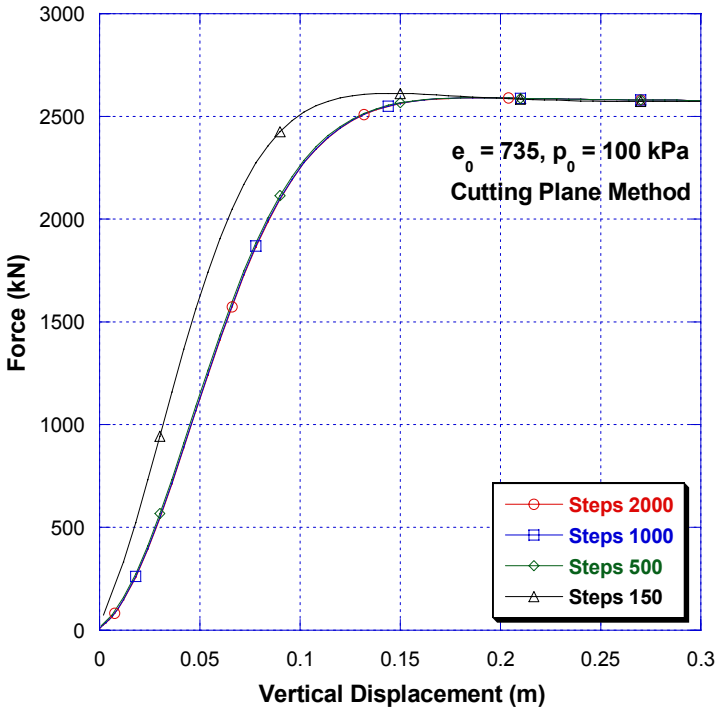

(a)

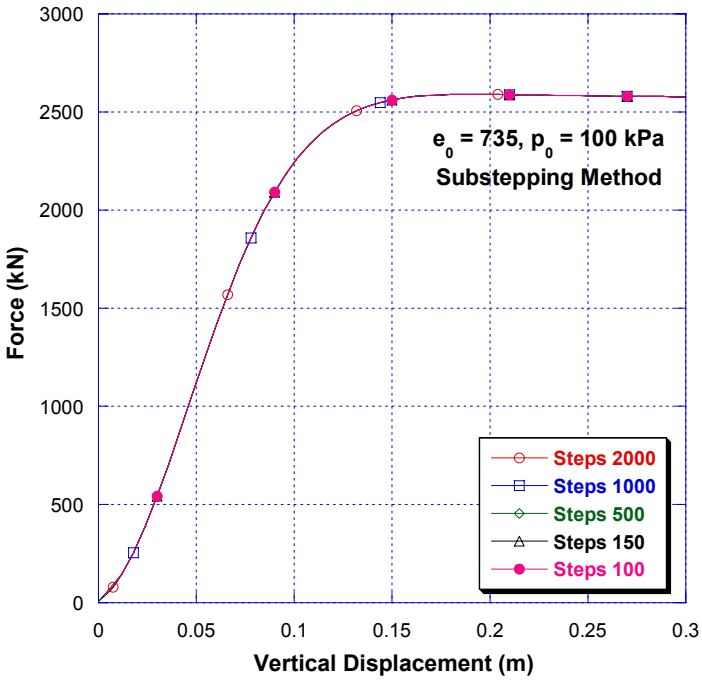

(b)

Figure 4. Force-displacement plots for undrained triaxial compression simulations using a micropolar model: (a) Cutting-Plane Method, (b) Substepping Method.

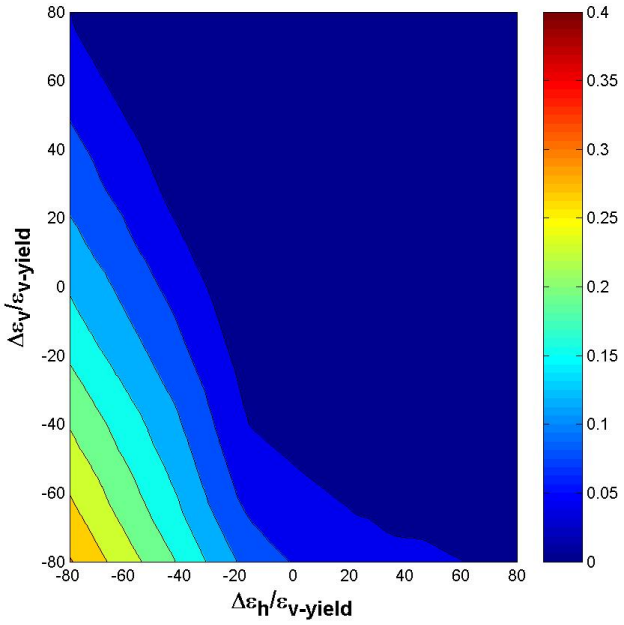

(a)

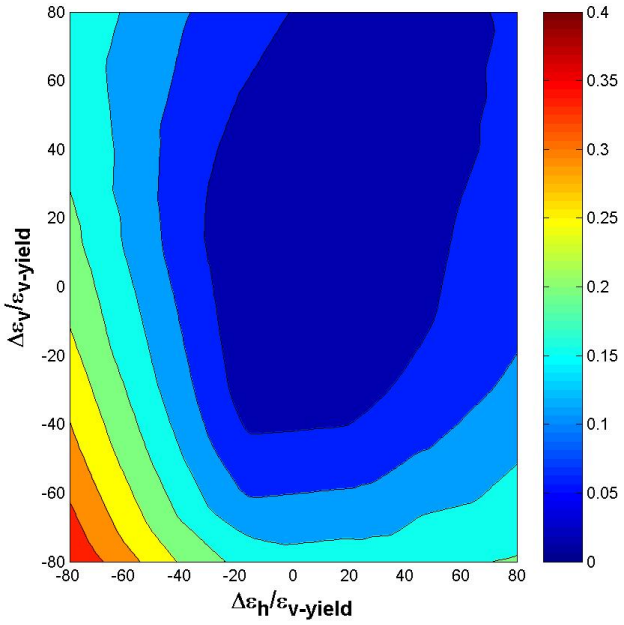

(b)

Figure 5. Comparison of iso-error map for biaxial compression simulations using a micropolar model: (a) Substepping Method, (b) Cutting-Plane Method.

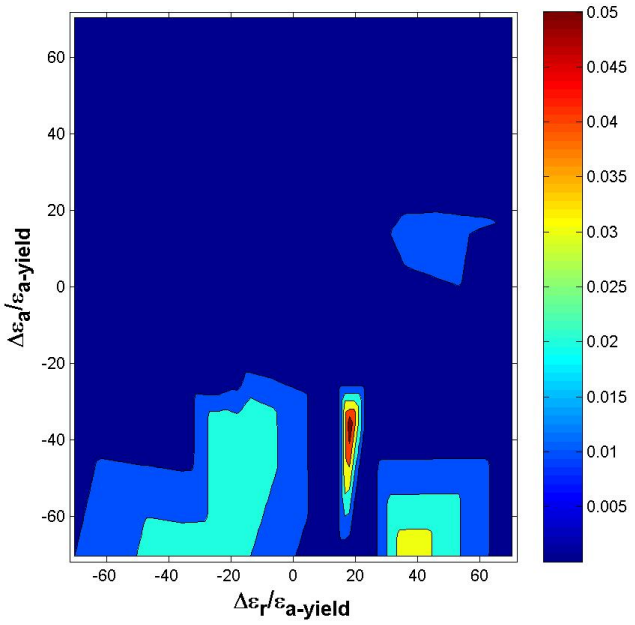

(a)

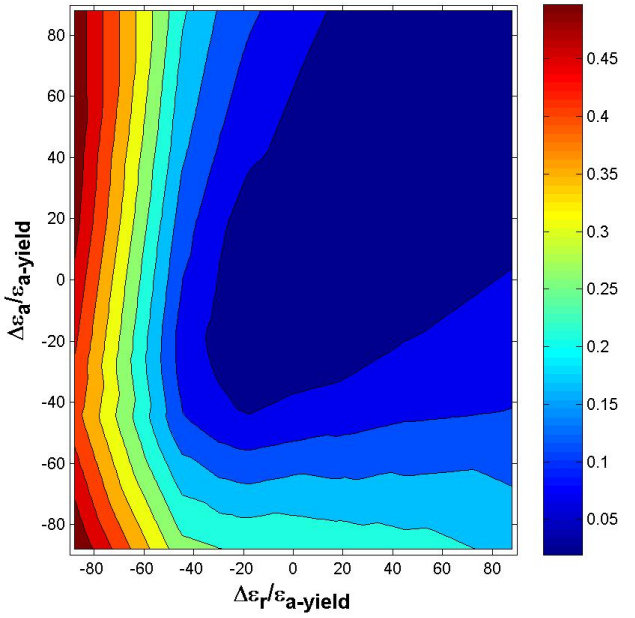

(b)

Figure 6. Comparison of iso-error map for triaxial compression simulations using a micropolar model: (a) Substepping Method, (b) Cutting-Plane Method.

For the triaxial simulations substepping method has relatively smaller error than that of cutting-plane method. The largest error 0.05% for substepping method occurs in the region where the radial strain increments are about 20 times the axial yield strain, and the axial strain increments are between 30 to 40 times the axial yield strain. In the case of cutting-plane method 0.5% error takes place in two zones: one where both the axial and radial strain increments are in tension and greater than 75 and 80 times the axial yield strain, and second where the axial strain increment is greater than 10 times axial yield strain in compression, and radial strain increments are greater than 80 times the axial yield strain in tension.

Considering all the comparisons of the performance of the two integration schemes, it is observed that substepping approach is clearly more robust than the cutting plane method.

5.2. Biaxial compression simulations

For the biaxial compression tests, a 4^{cm}x14^{cm} specimen of Toyoura sand is considered as shown in Figure 7. The finite element meshes used in these simulations consisted of 228 elements.

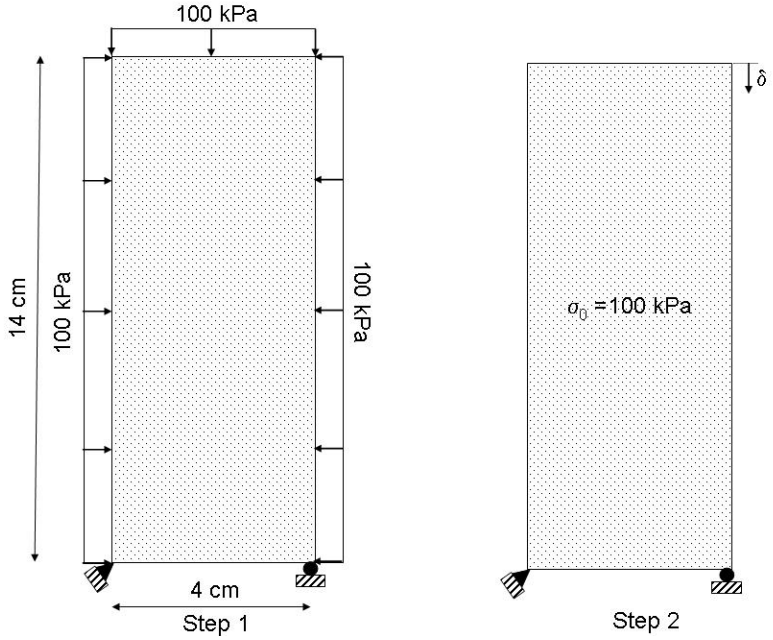

Figure 7. Biaxial specimen boundary conditions and simulation steps.

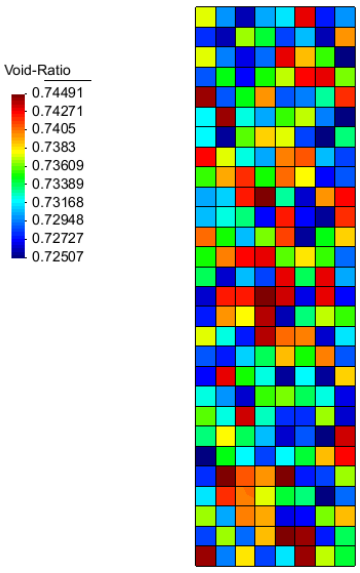

Figure 8. Random distribution of initial void ratio within the specimen.

These simulations were conducted for a relatively dense specimen of Toyoura sand that is slightly heterogeneous with an average initial void ratio of 0.735 (Dr = 63%). Initial void ratios at different integration points within the elements were randomly assigned using a

random number generator. The average void ratio is 0.735 with a variance of 0.01. The random distribution of initial void ratios within the specimen is shown in Figure 8. The values of initial void ratios vary from 0.725 to 0.745. All non-polar model parameters are the same as those proposed in Dafalias and Manzari [2] for Toyoura sand.

The boundary conditions and simulation steps are shown in Figure 7. The micro-rotations (ϕ_z) at the top and bottom edges of the specimen are set to zero. The specimen is isotropically consolidated first by applying a confining pressure of 100 kPa, and then it is sheared by applying a vertical displacement of 3 cm on the top edge.

Biaxial compression simulations in drained and globally undrained conditions were conducted by using substepping and cutting-plane algorithms. In drained simulations a length scale of $l_1=l_2=4$ mm is used, and in undrained simulations a length scale of $l_1=l_2=1$ mm. In undrained biaxial simulations the pore water is prevented from seeping out of the boundaries of the soil specimen, but it is allowed to flow within the specimen. Therefore, it is undrained in a global sense.

Figure 9 shows the force-displacement plot for drained simulations using the two integration schemes. The simulation using substepping method successfully completes while the simulation using cutting plane method fails at the peak of the force-displacement curve, i.e., at the onset of strain localization. The solution does not converge regardless of the step size used. This divergence problem is caused by the accumulation of the drift-off errors which is due to the weak enforcement of the consistency condition used in the cutting-plane algorithm. The force-displacement curve using the cutting-plane method is identical to that obtained by using the substepping method up to the point where the former fails. Note that because the size of the yield surface for this model is small the specimen undergoes plastic deformation in a relatively few steps.

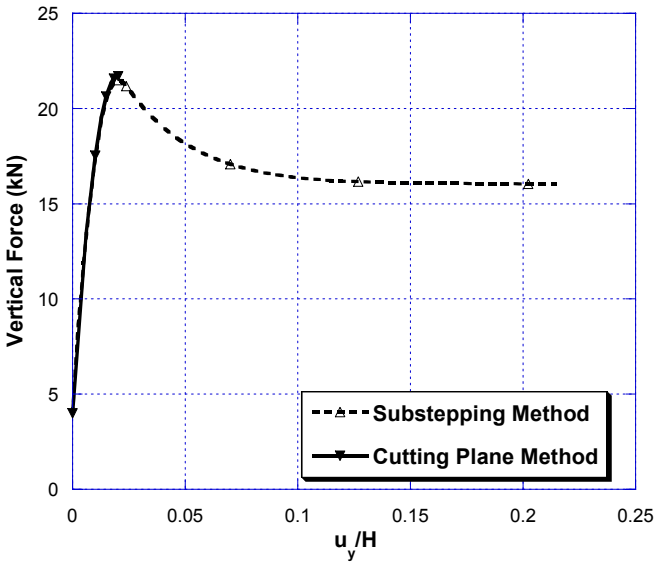

Figure 9. Force-displacement curves for drained biaxial simulations using the two integration schemes.

The contours of micro-rotation at the peak in drained simulations using the two integration schemes are shown in Figure 10. The localized band is not yet formed at this point. The distribution of the micro-rotation within the specimen is similar.

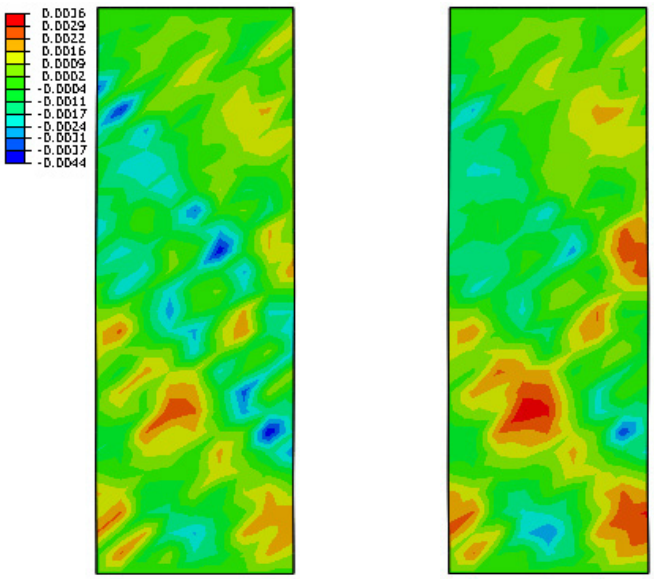

Figure 10. Contours of micro-rotation at the peak in drained biaxial simulations for: (a) Substepping Method, (b) Cutting-Plane Method.

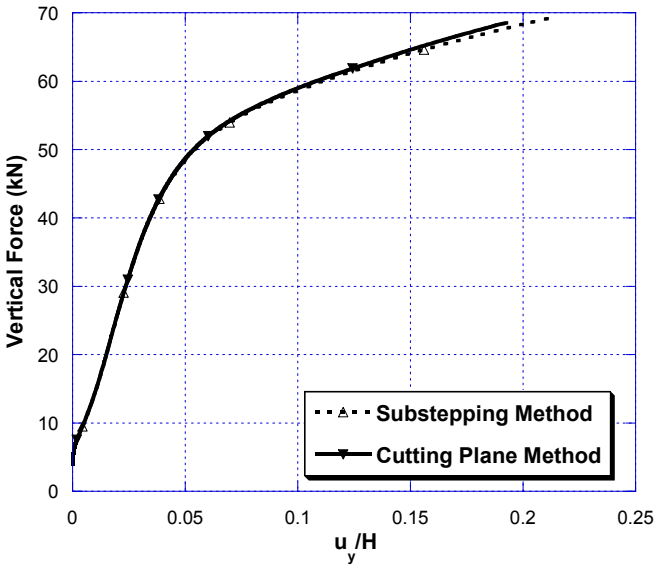

Figure 11. Force-displacement curves for undrained biaxial simulations using the two integration schemes.

Figure 11 shows the force-displacement plots for the two integrations schemes for the undrained simulations. The simulation using the cutting plane method converges up to about 90% of the prescribed vertical displacement. The force-displacement curve of the cutting plane method slightly deviates from that of the substepping method after 15% nominal strain. This might be because no drift-off errors correction is used for the cutting plane algorithm.

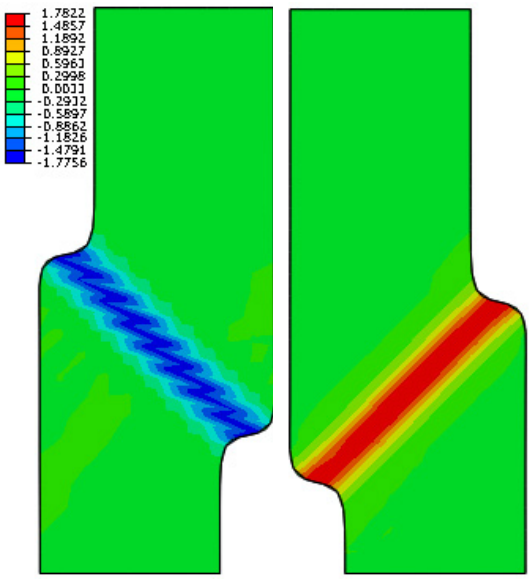

Figure 12. Contours of micro-rotation in undrained biaxial simulations for: (a) Substepping Method, (b) Cutting-Plane Method.

The contours of micro-rotation for the undrained simulations using the substepping and cutting plane schemes, up to where the latter fails, are shown in Figure 12. The shear localization modes obtained from the two simulations are similar, but due to the random nature of shear band formation directions of the bands are mirror images of one another. In the case using substepping method the localized band cuts the specimen diagonally from left to right edge where the band initiates at the center of the left edge. In the case using cutting plane method the localized band initiates at the center of the right edge and the band crosses diagonally from right to left edge. The micro-rotations within the shear band using the two schemes are of the same magnitude (about 102 degrees), but in opposite directions (counterclockwise for substepping method and clockwise for cutting plane method). The thickness and the inclination of the band with respect to horizontal axis are the same for the two simulations.

The CPU usage for the undrained biaxial simulations using the two integration schemes is shown in Table 1. Cutting plane method requires much smaller step size compared to the substepping method for the solution to converge which adds computational cost. Even though the simulation using cutting plane method completes only up to 90% of the prescribed displacement its CPU usage is over twice that of the substepping method. Clearly, for simulations of larger problems the substepping method is much more efficient than the cutting plane method.

Table 1. CPU usage for undrained biaxial simulations.

Algorithm	Global Iterations	CPU (sec)
Substepping	5193	6424
Cutting Plane	11472	12129

6. Conclusion

The micropolar plasticity model proposed by Manzari and Dafalias [3] is integrated using substepping and cutting plane methods. The performances of the two integration schemes are

compared in a series of one-element simulations as well as biaxial compression tests on slightly heteregenous specimens of Toyoura sand. Both cases show that the performance of the substepping method is superior to that of the cutting-plane method. In strain localization problem, where the cutting-plane method faces convergence difficulties, the substepping method is able to produce complete solution at a lesser computational cost.

Acknowledgement

This work is supported by the National Science Foundation Geomechanics and Geohazard programs directed by Dr. Richard Fragaszy. This support is gratefully acknowledged.

References

[1] M.T. Manzari, Y.F. Dafalias, A two-surface critical plasticity model for sand, *Geotechnique*, Vol. 47, 2 (1997) 255-272.

[2] Y.F. Dafalias, M.T. Manzari, Simple plasticity sand model accounting for fabric change effects, *Journal of Engineering Mechanics*, Vol. 130, 6 (2004) 622-634.

[3] M.T. Manzari, Y.F. Dafalias, A critical state two-surface micropolar plasticity model for sands, *Proceedings of 11th International Conference on Fracture*, Turin, Italy, (March 2005).

[4] M. Ortiz, J.C. Simo, An analysis of a new class of integrations algorithms for elasto-plastic constitutive relations, *International Journal for Numerical Methods in Engineering*, Vol. 23 (1986) 353-366.

[5] K. Runesson, Implicit integration of elastoplastic relations with reference to silts. Short Communication, *International Journal for Numerical and Analytical Methods in Geomechanics*, Vol. 11 (1987) 315-321.

[6] A. Gens, D.M. Potts, Critical state models in computational geomechanics, *Engineering Computations*, Vol. 5 (1987) 178-197.

[7] R.I. Borja, S.R. Lee, Cam-clay plasticity. Part I: implicit integration of elasto-plastic constitutive relations, *Computer Methods in Applied Mechanics and Engineering*, Vol. 78 (1990) 49-72.

[8] Y.M.A. Hashash, A.J. Whittle. Integration of the modified Cam-clay model in non-linear finite element analysis, *Computers and Geotechniques*, Vol. 14 (1992) 59-83.

[9] M. Rouainia, D.M. Wood, Implicit numerical integration for a kinematic hardeining soil plasticity model, *International Journal for Numerical and Analytical Methods in Geomechanics*, Vol. 25 *(*2001) 1305-1325.

[10] M.T. Manzari, R. Prachathananukit, On integration of a cyclic soil plasticity model. *International Journal for Numerical and Analytical Methods in Geomechanics*, Vol. 25 (2001) 525-549.

[11] S.W. Sloan, Substepping schemens for the numerical integration of elastoplastic stress-strain relations, *International Journal for Numerical Methods in Engineering*, Vol. 24 (1987) 893-911.

[12] S.W. Sloan, A.J. Abbo, D. Sheng, Refined explicit integration of elastoplastic models with automatic error control, *Engineering Computations*, Vol. 18, 1/2 (2001) 121-154.

[13] J. Zhao et al, Explicit stress integration of complex soil models, *International Journal for Numerical and Analytical Methods in Geomechanics*, Vol. 29 (2005) 1209-1229.

[14] M. Sanchez et al, Implementation algorithm of a generalized plasticity model for swelling clays, *Computers and Geotechniques*, Vol. 35 (2008) 860-871.

[15] K.I. Andrianopoulos, A.G. Papadimitriou, G.D. Bouckovalas, Explicit integration of bounding surface model for the analysis of earthquake soil liquefaction*, International Journal for Numerical and Analytical Methods in Geomechanics*, Vol. 34 (2010) 1586-1614.

[16] J. Zhao, D. Sheng, S.W. Sloan, Explicit stress integration of complex soil models, *International Journal for Numerical Methods in Engineering* Vol. 29 (2005) 1209-1229.

[17] J.C. Simo, M. Ortiz, A unified approach to finite deformation elastoplastic analysis based on the use of hyper-elastic constitutive equations, *Computer Methods in Applied Mechanics and Engineering*, Vol. 49 (1985) 221-245.

[18] W. Nowacki W, *Theory of Asymmetric Elasticity*, Pergamon Press, New York, 1986.

[19] I. Vardoulakis, J. Sulem, *Bifurcation Analysis in Geomechanics*, Blackie Academic and Professional, Chapman and Hall, Glasgow, 1995.

Appendix-A

The general elastic stress-strain relationship is given by:

$$\hat{\sigma}_{ij} = \hat{D}^e_{ijkl}\hat{\varepsilon}^e_{ij}; \quad \hat{\boldsymbol{\sigma}} = \hat{\mathbf{D}}^e : \hat{\boldsymbol{\varepsilon}}^e \tag{A1}$$

Here the stresses and strains are asymmetric. For plane strain and axisymmetric case we can write the stress-strain relationship as:

$$\begin{bmatrix} \sigma_{xx} \\ \sigma_{yy} \\ \sigma_{zz} \\ \sigma_{xy} \\ \sigma_{yx} \\ \mu_{xz} \\ \mu_{yz} \end{bmatrix} = \begin{bmatrix} \bar{K}+\frac{4}{3}\bar{G} & \bar{K}-\frac{2}{3}\bar{G} & \bar{K}-\frac{2}{3}\bar{G} & 0 & 0 & 0 & 0 \\ \bar{K}-\frac{2}{3}\bar{G} & \bar{K}+\frac{4}{3}\bar{G} & \bar{K}-\frac{2}{3}\bar{G} & 0 & 0 & 0 & 0 \\ \bar{K}-\frac{2}{3}\bar{G} & \bar{K}-\frac{2}{3}\bar{G} & \bar{K}+\frac{4}{3}\bar{G} & 0 & 0 & 0 & 0 \\ 0 & 0 & 0 & \bar{G}+G_c & \bar{G}-G_c & 0 & 0 \\ 0 & 0 & 0 & \bar{G}-G_c & \bar{G}+G_c & 0 & 0 \\ 0 & 0 & 0 & 0 & 0 & 2\bar{\gamma} & 0 \\ 0 & 0 & 0 & 0 & 0 & 0 & 2\bar{\gamma} \end{bmatrix} \begin{bmatrix} \varepsilon_{xx} \\ \varepsilon_{yy} \\ \varepsilon_{zz} \\ \varepsilon_{xy} \\ \varepsilon_{yx} \\ \kappa_{xz} \\ \kappa_{yz} \end{bmatrix} \tag{A2}$$

Here:

$$\hat{\mathbf{D}}^e = \begin{bmatrix} \bar{K}+\frac{4}{3}\bar{G} & \bar{K}-\frac{2}{3}\bar{G} & \bar{K}-\frac{2}{3}\bar{G} & 0 & 0 & 0 & 0 \\ \bar{K}-\frac{2}{3}\bar{G} & \bar{K}+\frac{4}{3}\bar{G} & \bar{K}-\frac{2}{3}\bar{G} & 0 & 0 & 0 & 0 \\ \bar{K}-\frac{2}{3}\bar{G} & \bar{K}-\frac{2}{3}\bar{G} & \bar{K}+\frac{4}{3}\bar{G} & 0 & 0 & 0 & 0 \\ 0 & 0 & 0 & \bar{G}+G_c & \bar{G}-G_c & 0 & 0 \\ 0 & 0 & 0 & \bar{G}-G_c & \bar{G}+G_c & 0 & 0 \\ 0 & 0 & 0 & 0 & 0 & 2\bar{\gamma} & 0 \\ 0 & 0 & 0 & 0 & 0 & 0 & 2\bar{\gamma} \end{bmatrix} \tag{A3}$$

in which:

$$\bar{K} = \frac{\left(\sqrt{p}+\frac{\bar{K}_0\Delta\varepsilon_v}{2\sqrt{p_{at}}}\right)^2 - p}{\Delta\varepsilon_v}; \quad \bar{G} = \frac{3(1-2\nu)}{2(1+\nu)}\bar{K}; \quad 2\bar{\gamma} = \frac{4\bar{G}G_c}{\bar{G}+G_c}\ell_1^2 \tag{A4}$$

$$\bar{K}_0 = \frac{3(1-2\nu)}{2(1+\nu)}G_0 p_{at}\frac{(2.97-e)^2}{1+e}\sqrt{\frac{p}{p_{at}}} \tag{A5}$$